3-2017

Vibration properties of and power harvested by a system of electromagnetic vibration energy harvesters that have electrical dynamics

Christopher G. Cooley
Department of Mechanical Engineering and Energy Processes, chris.cooley@siu.edu

Recommended Citation

Cooley, Christopher G. "Vibration properties of and power harvested by a system of electromagnetic vibration energy harvesters that have electrical dynamics." *Mechanical Systems and Signal Processing* 94 (Mar 2017): 237-252. doi:10.1016/j.ymssp.2017.02.038.

Vibration Properties of and Power Harvested by a System of Electromagnetic Vibration Energy Harvesters That Have Electrical Dynamics

- Manuscript -

Christopher G. Cooley*

Department of Mechanical Engineering and Energy Processes

Southern Illinois University Carbondale

1230 Lincoln Dr.

Carbondale, IL 62901, USA

February 8, 2017

---

*Corresponding author: chris.cooley@siu.edu

Abstract

This study investigates the vibration and dynamic response of a system of coupled electromagnetic vibration energy harvesting devices that each consist of a proof mass, elastic structure, electromagnetic generator, and energy harvesting circuit with inductance, resistance, and capacitance. The governing equations for the coupled electromechanical system are derived using Newtonian mechanics and Kirchhoff circuit laws for an arbitrary number of these subsystems. The equations are cast in matrix operator form to expose the device's vibration properties. The device's complex-valued eigenvalues and eigenvectors are related to physical characteristics of its vibration. Because the electrical circuit has dynamics, these devices have more natural frequencies than typical electromagnetic vibration energy harvesters that have purely resistive circuits. Closed-form expressions for the steady state dynamic response and average power harvested are derived for devices with a single subsystem. Example numerical results for single and double subsystem devices show that the natural frequencies and vibration modes obtained from the eigenvalue problem agree with the resonance locations and response amplitudes obtained independently from forced response calculations. This agreement demonstrates the usefulness of solving eigenvalue problems for these devices. The average power harvested by the device differs substantially at each resonance. Devices with multiple subsystems have multiple modes where large amounts of power are harvested.

1 Introduction

Vibration energy harvesting research is reviewed in Refs. [1–4].

Vibration energy harvesting from electromagnetic devices has been investigated in Refs. [5–27]. Stephen [7] analyzed the dynamic response of and power generated by devices with a single proof mass and purely resistive electrical load.

When operated near resonance, these devices harvest maximum power when the damping from the electrical circuit equals that in the mechanical system. Mann and Sims [8] investigated the effect of coil inductance on the response and power harvested by electromagnetic vibration energy harvesters. The power generated from sinusoidal, periodic, and random excitation was determined. Mann and Sims [9] studied the nonlinear dynamics of a magnetically levitating vibration energy harvester. Yang et al. [10] experimentally investigated the energy harvested from the first three modes of a vibrating beam electromagnetic device. Mann and Owens [11] investigated the response and energy harvested by a nonlinear electromagnetic device. Trimble et al. [12] developed and analyzed a vibration energy harvester for spinning systems that experience rotational vibrations. Cammarano et al. [13] studied vibration energy harvesting from electromagnetic devices that can be actively tuned for improved performance. Elvin and Elvin [15] analytically and experimentally investigated the power generated by an electromagnetic vibration energy harvester. Their model accurately predicted the dynamic response compared to experiments for a wide range of system parameters. Daqaq [16] investigated the power harvested by bistable nonlinear electromagnetic vibration energy harvesters excited by random vibration. Tang and Zuo [17] investigated vibration energy harvesting from a dual-mass device that consists of two proof masses coupled by an electromagnetic generator or piezoelectric structure. The dual-mass device was shown to outperform comparable devices with a single mass. Vibration energy harvesting from dual-mass devices subjected to random excitation was investigated in Ref. [21]. The energy harvested from the vibration of rectangular plates with an arbitrary number of electromagnetic vibration energy harvesters was investigated by Harne [22]. He and Daqaq [23] studied vibration energy harvesting from nonlinear devices with asymmetric potential function asymmetries. Gonzalez-Buelga et al. [24] analyzed a tunable electromagnetic vibration absorber that converts the absorbed vibration into electrical power. Caruso [25] investigated the power harvested by electromagnetic vibration energy harvesters with electrical circuits that have inductance, capacitance, and resistance. When adaptively tuned at each frequency, this device has broadband energy harvesting ability. Tang et al. [28] investigated the energy harvesting and vibration damping abilities of shunted tuned mass dampers. Many of these studies focus on maximizing the power harvested by the devices. None of these works investigate the vibration properties of electromagnetic vibration energy harvesters, which is a focus of this work. Most of the electromagnetic devices referenced above are designed to power a single electrical load. This work analyzes electromagnetic devices that can simultaneously power multiple electrical loads.

Piezoelectric stack vibration energy harvesting devices have been investigated in Refs. [29–33]. Vibrating beam devices with piezoelectric material layers have been investigated in Refs. [30, 34–40], for example. Many more can be found in the review articles in Refs. [1–4]. Piezoelectric vibration energy harvesters with multiple proof masses and degrees of freedom are investigated in Refs. [41–43].

This study investigates the vibration properties of electromagnetic vibration energy harvesters. The governing equations are derived for devices with an arbitrary number of energy harvesting subsystems, which each consist of a proof mass, elastic structure, and an energy harvesting circuit with inductance, resistance, and capacitance. The device's eigenvalue problem is cast in matrix operator form, which makes clear the qualitative nature of the vibration of these devices. Numerical results are generated for example devices with one and two subsystems. Dynamic response predictions are compared to natural frequency and vibration mode results obtained from the eigenvalue problem. The power harvested from sinusoidal base excitation is determined for a wide range of excitation frequencies. The different resonances of the device are compared to determine the preferred modes for energy harvesting applications. The natural frequencies, dynamic response, and power harvested are calculated for a wide range of electric circuit model parameters.

2 Analysis

2.1 Analytical model

A schematic of the electromagnetic vibration energy harvester is shown in Fig. 1. The device consists of N energy harvesting subsystems. Each subsystem has a proof mass m_i ($i = 1, 2, \ldots, N$) and an energy harvesting circuit. Adjacent proof masses are connected by (i) elastic structures that have stiffnesses k_i and equivalent viscous damping coefficients c_i and (ii) electromagnetic generators with electromechanical coupling coefficients κ_i. The first proof mass is attached to a vibrating host system with prescribed translational motion $y(t)$. The relative deflections of the proof masses with respect to the motion of the host system are $x_i(t)$. Their absolute motions are $X_i(t) = y(t) + x_i(t)$. Each proof mass is dynamically excited by an applied force $f_i(t)$. We assume these are fluctuating forces that have vanishing mean components.

The electromagnetic generators provide input voltage to the energy harvesting circuits. Because there are multiple energy harvesting circuits, this device has the ability to power multiple electrical loads. Each circuit has inductance L_i, capacitance C_i, and resistance R_i. In some devices, the circuit's inductance comes from the coil in the electromagnetic generator [6,8,13,15]. Formulas for calculating the inductance and electromagnetic coupling coefficient for a given electromagnetic generator can be found in Ref. [15]. The resistances R_i represent the equivalent resistance in the circuit. The majority of R_i is due to the electrical load powered by the device, e.g., a sensor or other electronics. Additional resistance may occur due to the circuit itself. In many devices this internal circuit resistance is significantly lower than the load resistance and is neglected. The capacitance is an added element to the circuit, although an electrical load may have capacitance, like in Ref. [13]. For the passive vibration energy harvesting devices investigated in this work all of the inductances, resistances, and capacitances are fixed.

Relative velocity between the ends of the electromagnetic generators provide input voltage to the energy harvesting circuits according to

$$V_i = \begin{cases} \kappa_i \dot{x}_i, \quad i = 1 \\ \kappa_i \left(\dot{x}_i - \dot{x}_{i-1} \right), \quad 1 < i \leq N. \end{cases} \tag{1}$$

The electromagnetic generators apply electromotive forces $F_i = \kappa_i \dot{q}_i$ on the proof masses.

The use of Newtonian mechanics gives the governing equations for each proof mass as

$$m_1 \ddot{x}_1 + (c_1 + c_2)\dot{x}_1 - c_2 \dot{x}_2 + (k_1 + k_2)x_1 - k_2 x_2 + F_1 - F_2 = f_1 - m_1 \ddot{y}, \tag{2a}$$

$$\begin{aligned} m_i \ddot{x}_i - c_i \dot{x}_{i-1} + (c_i + c_{i+1})\dot{x}_i - c_{i+1}\dot{x}_{i+1} - k_i x_{i-1} + (k_i + k_{i+1})x_i - k_{i+1} x_{i+1} + F_i \\ - F_{i+1} = f_i - m_i \ddot{y}, \quad 1 < i < N, \end{aligned} \tag{2b}$$

$$m_N \ddot{x}_N - c_N \dot{x}_{N-1} + c_N \dot{x}_N - k_N x_{N-1} + k_N x_N + F_N = f_N - m_N \ddot{y}. \tag{2c}$$

The use of Kirchhoff's voltage law for each energy harvesting circuit gives

$$L_i \ddot{q}_i + R_i \dot{q}_i + \frac{1}{C_i} q_i - V_i = 0, \quad i = 1, 2, \ldots, N. \tag{3}$$

The governing equations for the device consist of Eq. (2) for the mechanical degrees of freedom and Eq. (3) for the electrical degrees of freedom. Coupling occurs in these equations between the proof mass velocities ($\dot{x}_i$) and the electric circuit currents ($\dot{q}_i$). Adjacent proof masses are coupled by the discrete stiffness and damping elements.

For devices that consist of a single subsystem, the equation governing the motion of the mass can be reduced from Eq. (2a) by requiring the quantities c_2, k_2, F_2, and x_2 vanish. The electrical charge is governed by Eq. (3) with $i = 1$. Use of the electromagnetic generator force $F_1 = \kappa_1 \dot{q}_1$ and voltage $V_1 = \kappa_1 \dot{x}_1$ into those results gives the electromechanically coupled equations of motion for the device as

$$m_1 \ddot{x}_1 + c_1 \dot{x}_1 + \kappa_1 \dot{q}_1 + k_1 x_1 = f_1 - m_1 \ddot{y}, \tag{4a}$$

$$L_1 \ddot{q}_1 - \kappa_1 \dot{x}_1 + R_1 \dot{q}_1 + \frac{1}{C_1} q_1 = 0. \tag{4b}$$

Equations (4) agree with those derived in Ref. [25] for vanishing base motion. The equation given in Ref. [13] for the mechanical system agrees with Eq. (4a) for vanishing applied force f_1. The equation for the electrical system in Eq. (4b), however, differs with that given in Ref. [13] because in that work the equation is expressed in terms of the circuit in the current. Substitution of the current $I = \dot{q}_1$ into Eq. (4b) and use of $q_1(t) = \int_0^t I(\tau) d\tau$ gives

$$L_1 \dot{I} - \kappa_1 \dot{x}_1 + R_1 I + \int_0^t \frac{I(\tau)}{C_1} d\tau = 0, \tag{5}$$

which agrees with that given in Ref. [13].

For purely resistive energy harvesting circuits (i.e., for vanishing inductances ($L_i \to 0$) and large capacitances ($C_i \to \infty$) so that the voltage drops across these elements are negligible), Eq. (3) gives the electrical current $\dot{q}_i = V_i / R_i$. The use of this result and Eq. (1) into Eq. (2) gives

$$m_1\ddot{x}_1 + \left(c_1 + c_2 + \frac{\kappa_1^2}{R_1} + \frac{\kappa_2^2}{R_2}\right)\dot{x}_1 - \left(c_2 + \frac{\kappa_2^2}{R_2}\right)\dot{x}_2 + (k_1 + k_2)x_1 - k_2 x_2$$
$$= f_1 - m_1\ddot{y}, \quad \text{(6a)}$$

$$m_i\ddot{x}_i - \left(c_i + \frac{\kappa_i^2}{R_i}\right)\dot{x}_{i-1} + \left(c_i + c_{i+1} + \frac{\kappa_i^2}{R_i} + \frac{\kappa_{i+1}^2}{R_{i+1}}\right)\dot{x}_i - \left(c_{i+1} + \frac{\kappa_{i+1}^2}{R_{i+1}}\right)\dot{x}_{i+1}$$
$$- k_i x_{i-1} + (k_i + k_{i+1})x_i - k_{i+1}x_{i+1} = f_i - m_i\ddot{y}, \quad 1 < i < N, \quad \text{(6b)}$$

$$m_N\ddot{x}_N - \left(c_N + \frac{\kappa_N^2}{R_N}\right)\dot{x}_{N-1} + \left(c_N + \frac{\kappa_N^2}{R_N}\right)\dot{x}_N - k_N x_{N-1} + k_N x_N = f_N - m_N\ddot{y}. \quad \text{(6c)}$$

For dual-mass devices ($N = 2$) with a single electrical circuit between the two masses and applied forced excitation, Eq. (6) agrees with that derived in Ref. [17] for vanishing c_1, κ_1, f_2, and y. For similar dual-mass devices with base excitation, Eq. (6) differs with Ref. [17] because in that work the equations are cast in terms of absolute deflections, whereas Eq. (6) uses deflections relative to the host system's motion $y(t)$. For devices with purely resistive electrical circuits, Eq. (6) shows that the impact of electromechanical coupling is similar to that for viscous mechanical damping. These devices will have resonances at excitation frequencies near the corresponding undamped mechanical systems's natural frequencies, provided the total damping in the system is sufficiently small. For electrical circuits that contain both inductance and capacitance, however, the governing equations include dynamics in both the mechanical (Eq. (2)) and electrical systems (Eq. (3)). This electromechanical coupling strongly impacts the device's dynamics, which will be demonstrated in the Results section.

Equations (2) and (3) are nondimensionalized using the nondimensional parameters

$$\hat{t} = \sqrt{\frac{k_1}{m_1}}t, \quad \hat{x}_i = \frac{x_i}{Y_0}, \quad \hat{y} = \frac{y}{Y_0}, \quad \hat{f}_i = \frac{f_i}{k_1 Y_0}, \quad \hat{q}_i = \frac{\kappa_1}{Y_0\sqrt{k_1 m_1}}q_i, \quad \mu_i = \frac{m_i}{m_1},$$
$$\zeta_i = \frac{c_i}{\sqrt{k_1 m_1}}, \quad \xi_i = \frac{k_i}{k_1}, \quad \nu_i = \frac{\kappa_i}{\kappa_1}, \quad \alpha_i = \frac{L_i k_1}{\kappa_1^2}, \quad \beta_i = \frac{R_i\sqrt{k_1 m_1}}{\kappa_1^2}, \quad \gamma_i = \frac{m_1}{C_i \kappa_1^2}, \tag{7}$$

where Y_0 is the amplitude of the host system's motion in the case of base excitation. In cases when the base motion vanishes and the device is excited by applied forces, we choose Y_0 to be the static deflection of the first proof mass. The resulting nondimensional equations in matrix operator form are

$$\mathbf{M}\ddot{\mathbf{u}} + (\mathbf{D} + \mathbf{E})\,\dot{\mathbf{u}} + \mathbf{K}\mathbf{u} = \mathbf{F}(t), \tag{8}$$

$$\mathbf{u} = \left[x_1, q_1, x_2, q_2, \ldots, x_N, q_N\right]^T, \tag{9}$$

$$\mathbf{M} = \mathrm{diag}(\mu_1, \alpha_1, \mu_2, \alpha_2, \ldots, \mu_N, \alpha_N), \tag{10a}$$

$$\mathbf{D} = \begin{bmatrix} \zeta_1+\zeta_2 & 0 & -\zeta_2 & 0 & 0 & \ldots \\ 0 & \beta_1 & 0 & 0 & 0 & \ldots \\ -\zeta_2 & 0 & \zeta_2+\zeta_3 & 0 & -\zeta_3 & \ldots \\ 0 & 0 & 0 & \beta_2 & 0 & \ldots \\ 0 & 0 & -\zeta_3 & 0 & \zeta_3+\zeta_4 & \ldots \\ \vdots & \vdots & & \ldots & & \ddots \end{bmatrix}, \tag{10b}$$

$$\mathbf{E} = \begin{bmatrix} 0 & \nu_1 & 0 & -\nu_2 & 0 & \ldots \\ -\nu_1 & 0 & 0 & 0 & 0 & \ldots \\ 0 & 0 & 0 & \nu_2 & 0 & \ldots \\ \nu_2 & 0 & -\nu_2 & 0 & 0 & \ldots \\ 0 & 0 & 0 & 0 & 0 & \ldots \\ \vdots & \vdots & & \ldots & & \ddots \end{bmatrix}, \tag{10c}$$

$$\mathbf{K} = \begin{bmatrix} \xi_1+\xi_2 & 0 & -\xi_2 & 0 & 0 & \dots \\ 0 & \gamma_1 & 0 & 0 & 0 & \dots \\ -\xi_2 & 0 & \xi_2+\xi_3 & 0 & -\xi_3 & \dots \\ 0 & 0 & 0 & \gamma_2 & 0 & \dots \\ 0 & 0 & -\xi_3 & 0 & \xi_3+\xi_4 & \dots \\ \vdots & \vdots & & \dots & & \ddots \end{bmatrix}, \tag{10d}$$

$$\mathbf{F} = \left[f_1 - \mu_1 \ddot{y}, 0, f_2 - \mu_2 \ddot{y}, 0, \dots, f_N - \mu_N \ddot{y}, 0\right]^T, \tag{10e}$$

where the hats on all nondimensional parameters have been removed for brevity and the overdot here, and in the remainder of the paper, denotes nondimensional time differentiation. The mass $\mathbf{M}^T = \mathbf{M}$, damping $\mathbf{D}^T = \mathbf{D}$, and stiffness $\mathbf{K}^T = \mathbf{K}$ matrices are symmetric and positive-definite. The electromechanical coupling matrix $\mathbf{E}^T = -\mathbf{E}$ is skew-symmetric.

2.2 Free vibration

The eigenvalue problem comes from the substitution of the time-separable solution $\mathbf{u}(t) = \boldsymbol{\chi} e^{\lambda t}$ into the homogeneous form of Eq. (8) as

$$\lambda^2 \mathbf{M}\boldsymbol{\chi} + \lambda\left(\mathbf{D} + \mathbf{E}\right)\boldsymbol{\chi} + \mathbf{K}\boldsymbol{\chi} = \mathbf{0}, \quad \boldsymbol{\chi} = \left[X_1, Q_1, X_2, Q_2, \dots, X_N, Q_N\right]^T. \tag{11}$$

Equation (11) is a polynomial eigenvalue problem that has a total of $4N$ eigensolutions. The eigenvalues of Eq. (11) are generally complex-valued. This is seen by pre-multiplication of Eq. (11) by $\overline{\boldsymbol{\chi}}^T$ to get the polynomial expression

$$m\lambda^2 + (d + je)\lambda + k = 0, \tag{12}$$

where $m = \overline{\boldsymbol{\chi}}^T \mathbf{M} \boldsymbol{\chi}$, $d = \overline{\boldsymbol{\chi}}^T \mathbf{D} \boldsymbol{\chi}$, and $k = \overline{\boldsymbol{\chi}}^T \mathbf{K} \boldsymbol{\chi}$ are real-valued because the mass, damping, and stiffness matrices are real-valued and symmetric; they are positive because these matrices are positive-definite. The quantity $\overline{\boldsymbol{\chi}}^T \mathbf{E} \boldsymbol{\chi} = je$ (e is real-valued) is purely imaginary because of the skew-symmetry of the electromechanical coupling matrix $\mathbf{E}$. Note that Eq. (12) is not the characteristic equation associated with the eigenvalue problem in Eq. (11). The solution of Eq. (12) will give two, but not all, of the device's eigenvalues.

Solution of Eq. (12) using the quadratic formula gives

$$\lambda_{1,2} = -\frac{d + je}{2m} \pm \sqrt{\frac{(d + je)^2}{4m^2} - \frac{k}{m}}. \tag{13}$$

The imaginary parts of the eigenvalues λ are the real-valued natural frequencies of the device. The real parts of λ are the exponential decay or growth of the vibrations, depending on their sign. For vibration energy harvesters, the real parts of the eigenvalues are usually negative, indicating that the vibrations decay exponentially in time. When the eigenvalues of Eq. (11) are complex-valued, the eigensolutions come in complex-conjugate pairs. This can be seen by taking the complex-conjugate of Eq. (11) and noting that all matrices are real-valued. It is possible for some eigenvalues to be purely real-valued. Although Eq. (13) is helpful for explaining the qualitative nature of the device's eigenvalues, it is not used to calculate these eigenvalues because the eigenvectors are necessary to determine m, d, e, and k. All eigenvalue and eigenvector results shown in this work are numerically calculated from the matrix eigenvalue problem in Eq. (11).

The eigenvectors $\boldsymbol{\chi}$ have complex-valued elements. These physically represent phase differences between coordinates when the device vibrates in a single mode. Complex-valued eigenvectors are unique to within a change in amplitude and a shift in phase. Indeed, the eigenvector $\boldsymbol{\chi} \rightarrow a\boldsymbol{\chi}e^{j\theta}$, where a is an arbitrary real-valued amplitude and θ is an arbitrary real-valued angle, also satisfies the eigenvalue problem in Eq. (11). To make the eigenvectors unique we normalize them to have unit magnitude $\|\boldsymbol{\chi}\| = \sqrt{\overline{\boldsymbol{\chi}}^T \boldsymbol{\chi}} = 1$ and we select the phase shift so that the first proof mass's deflection X_1 is real-valued.

The free, single-mode response of the device is $\mathbf{u} = \boldsymbol{\chi} e^{\lambda t} + c.c. = 2\mathrm{Re}\left\{\boldsymbol{\chi} e^{\lambda t}\right\}$ (*c.c.* is the complex conjugate of the preceding terms). We express the eigenvalue in its real and imaginary parts as $\lambda = \tau + j\omega$, where τ and ω are real-valued constants. The vibration coordinate corresponding to the i^{th} mass can be written in polar form as $X_i = |X_i| e^{j\phi_i}$, where $|\cdot|$ denotes the magnitude of a complex-valued number and the phase angle ϕ_i is calculated from $\tan\phi_i = \mathrm{Im}(X_i)/\mathrm{Re}(X_i)$. Hence, the free vibration of the i^{th} mass, which is one element of free response vector $\mathbf{u}$, is given as $x_i(t) = 2|X_i| e^{\tau t} \cos(\omega t + \phi_i)$. This expression shows that the imaginary part of the eigenvalue ω is the natural frequency of the device in that mode. The real part of the eigenvalue τ, when negative, which is the typical case for vibration energy harvesters, determines the rate that the vibrations decay exponentially. The amplitudes and phases of the vibration are determined from the components of $\boldsymbol{\chi}$.

The properties of the vibration modes and their corresponding free, single-mode response are illustrated by a device with a single subsystem using the following dimensional parameters: $m = 1$ kg, $c = 50$ Ns/m, $k = 1$ kN/mm, $L = 2$ mH, $R = 0.5$ Ohm, and $C = 0.3$ mF. From the solution of the eigenvalue problem in Eq. (11) with these parameters, the device has two pairs of complex-conjugate eigenvalues $\lambda_1 = \overline{\lambda}_{-1} = -0.0366 + j0.828$ and $\lambda_2 = \overline{\lambda}_{-2} = -0.113 + j1.55$. The corresponding eigenvectors are also complex-conjugates, i.e., $\boldsymbol{\chi}_{-1,-2} = \overline{\boldsymbol{\chi}}_{1,2}$. The device's amplitude and phase normalized eigenvectors are shown in Figs. 2(a,b). The first eigenvector $\boldsymbol{\chi}_1$ (Fig. 2(a)) has meaningfully larger proof mass deflection than electric circuit charge. The magnitudes of deflection and charge are comparable in $\boldsymbol{\chi}_2$ (Fig. 2(b)). The sign of the phase of the electric circuit charge in each eigenvector differs. Figures 2(c,d) show the free, single-mode response in each mode. The vibrations decay exponentially as a result of the eigenvalues having negative real parts. The decay rates for each mode differ because of the differences in the magnitudes of the real parts of the eigenvalues. The oscillations in the second mode (Fig. 2(d)) are negligible after nearly eight oscillation cycles, whereas the first mode still has meaningful vibration after 10 oscillation cycles (Fig. 2(c)). The electric circuit charge lags the proof mass deflection in the free response of the first mode (Fig. 2(c)) because the phase of Q is positive (Fig. 2(a)). When the phase of Q is negative (like that for $\boldsymbol{\chi}_2$ in Fig. 2(b)) the deflection lags the electric circuit charge in single-mode free response (Fig. 2(d)).

2.3 Forced vibration

The dynamic excitation from applied loads $f_i = F_{0i}e^{j\omega t}$ and base motion $y = e^{j\omega t}$ is assumed to vary sinusoidally in time with nondimensional excitation frequency ω. The corresponding force vector $\mathbf{F}(t) = \mathbf{F}_0 e^{j\omega t}$, where $\mathbf{F}_0 = [F_{01} + \mu_1\omega^2, F_{02} + \mu_2\omega^2, \ldots, F_{0N} + \mu_N\omega^2]$ is a vector of known forcing amplitudes. The appropriate form of the steady state response for this excitation is $\mathbf{u}(t) = \mathbf{U}e^{j\omega t}$, where $\mathbf{U} = [X_1, Q_1, X_2, Q_2, \ldots, X_N, Q_N]^T$ is a vector of yet to be determined, complex-valued elements. Substitution of the complex-valued forms of $\mathbf{u}$ and $\mathbf{F}$ into Eq. (8) and solving for the response vector $\mathbf{U}$ gives

$$\mathbf{U} = \left[-\omega^2\mathbf{M} + j\omega\left(\mathbf{D} + \mathbf{E}\right) + \mathbf{K}\right]^{-1}\mathbf{F}_0. \tag{14}$$

The vibration of the masses and charges is determined from the calculated elements of $\mathbf{U}$. The deflection of the i^{th} mass is $x_i = X_i e^{j\omega t} = |X_i|e^{j(\omega t + \phi_i)}$, where the magnitude and phase shift are calculated as described earlier for free vibration. Similarly, the i^{th} charge is $q_i = Q_i e^{j\omega t} = |Q_i|e^{j(\omega t + \psi_i)}$, where $\tan\psi_i = \mathrm{Im}(Q_i)/\mathrm{Re}(Q_i)$. For cosine (sine) forcing the response is the real (imaginary) parts of these complex-valued expressions. The vibration amplitudes are given by the frequency response functions $|X_i|$ for the proof mass deflections and $|Q_i|$ for the electric circuit charges.

The power harvested by the device is the power dissipated by the resistance in each energy harvesting circuit, which, with use of Ohm's law, is given in nondimensional form as $P_i = \beta_i \dot{q}_i^2$. For cosine forcing, use of the current $\dot{q}_i = -\omega |Q_i| \sin(\omega t + \psi_i)$ into this expression and simplification using a trigonometric identity gives the harvested power as

$$P_i = \frac{\beta_i \omega^2 |Q_i|^2}{2} \left[1 - \cos(2\omega t + 2\psi_i)\right]. \tag{15}$$

The power harvested in each circuit consists of mean and sinusoidally fluctuating components. The fluctuations in Eq. (15) occur at twice the excitation frequency. The phase difference between the power and forcing is twice that between the electric circuit charge and forcing.

The average power harvested over one oscillation cycle is

$$\langle P_i \rangle = \frac{1}{T} \int_0^T P_i dt = \frac{\beta_i \omega^2 \left|Q_i\right|^2}{2}, \tag{16}$$

where $T = 2\pi/\omega$ is the oscillation period. We quantify the performance of the device by the average power harvested in each circuit given by Eq. (16).

3 Results

3.1 Single subsystem device

This section investigates the vibration of devices with a single subsystem (i.e., devices with one proof mass and one energy harvesting circuit) that are dynamically excited by nondimensional sinusoidal base motion $y(t) = \cos \omega t$. The applied dynamic excitation f_1 vanishes. The corresponding governing equations (obtained by reduction of Eq. (8) for $N = 1$) are

$$\begin{pmatrix} 1 & 0 \\ 0 & \alpha \end{pmatrix} \begin{pmatrix} \ddot{x} \\ \ddot{q} \end{pmatrix} + \left[\begin{pmatrix} \zeta & 0 \\ 0 & \beta \end{pmatrix} + \begin{pmatrix} 0 & 1 \\ -1 & 0 \end{pmatrix} \right] \begin{pmatrix} \dot{x} \\ \dot{q} \end{pmatrix} + \begin{pmatrix} 1 & 0 \\ 0 & \gamma \end{pmatrix} \begin{pmatrix} x \\ q \end{pmatrix} = \begin{pmatrix} \omega^2 \cos \omega t \\ 0 \end{pmatrix}, \tag{17}$$

where $\mu_1 = 1$, $\nu_1 = 1$, and $\xi_1 = 1$ from Eq. (7), $\zeta_2 = \xi_2 = 0$, and all subscripts have been removed for brevity.

The system analyzed in this section has dimensional parameters $m = 1$ kg, $c = 10$ Ns/m, $k = 1$ kN/mm, $\kappa = 30$ N/A, $L = 2$ mH, $R = 0.1$ Ohm, and $C = 0.3$ mF.

The eigenvalue problem associated with Eq. (17) has the general form given in Eq. (11). It is solved numerically using the above parameters for the for the eigenvalues λ and eigenvectors $\boldsymbol{\chi}$. This device has two pairs of complex-conjugate eigenvalues $\lambda_1 = \overline{\lambda}_{-1} = -0.00731 + j0.828$ and $\lambda_2 = \overline{\lambda}_{-2} = -0.0227 + j1.56$. The two natural frequencies are given by the imaginary parts of λ. They identify frequencies where large amounts of electrical power could potentially be harvested by the device. The decay rates of each eigenvalue (i.e., the real parts of λ) differ. The magnitudes and phases of the components of each eigenvector are shown in Fig. 3. Both eigenvectors have meaningful electromechanical coupling. We anticipate that the second mode ($\boldsymbol{\chi}_2$ in Fig. 3(b)) will perform better than the first ($\boldsymbol{\chi}_1$ in Fig. 3(a)) for vibration energy harvesting because the magnitude of the charge in $\boldsymbol{\chi}_2$ is nearly identical to that of the deflection.

Typical vibration energy harvesters with a single proof mass and electrical circuits with only resistance have one natural frequency [5–7]. The single subsystem device analyzed in this section has two natural frequencies because the circuit has both inductance and capacitance. These elements give dynamics in the electrical circuit. Neither natural frequency is near the corresponding uncoupled, purely mechanical system's natural frequency at $\omega = 1$ because of electromechanical coupling. These devices cannot be accurately modeled using a purely mechanical systems that neglect electromechanical coupling.

The dynamic response of the single subsystem device is solved in closed-form following the procedure given in Section 2.3. The resulting proof mass deflection and electric circuit charge frequency response functions are

$$|X| = \frac{\omega^2\sqrt{(\gamma-\alpha\omega^2)^2+\beta^2\omega^2}}{\sqrt{\left[(1-\omega^2)(\gamma-\alpha\omega^2)-(1+\zeta\beta)\omega^2\right]^2+\left[\beta\omega(1-\omega^2)+\zeta\omega(\gamma-\alpha\omega^2)\right]^2}}, \tag{18a}$$

$$|Q| = \frac{\omega^3}{\sqrt{\left[(1-\omega^2)(\gamma-\alpha\omega^2)-(1+\zeta\beta)\omega^2\right]^2+\left[\beta\omega(1-\omega^2)+\zeta\omega(\gamma-\alpha\omega^2)\right]^2}}. \tag{18b}$$

The dynamic response of the single subsystem device calculated from Eqs. (18) is shown in Fig. 4 for a wide range of excitation frequencies. The response calculations shown in Fig. 4 have been validated by results obtained by direct numerical integration of Eq. (17) (not shown). The device has two resonances that occur near its natural frequencies, which are calculated independently of the response problem using the eigenvalue problem in Eq. (11). The first resonance near $\omega = 0.828 \approx \mathrm{Im}(\lambda_1)$ has larger amplitude deflection than charge. This agrees qualitatively with the ratio of the magnitudes of the deflection and charge in $\boldsymbol{\chi}_1$ (Fig. 3(a)). At the second resonance near $\omega = 1.56 \approx \mathrm{Im}(\lambda_2)$ the amplitude of the proof mass deflection is only slightly larger than that of the electric circuit charge, which qualitatively agrees with the ratio of their magnitudes in $\boldsymbol{\chi}_2$ (Fig. 3(b)). The agreement between the dynamic response predictions and the eigenvalue problem results demonstrates the usefulness of the eigenvalue problem for these devices. Some dynamic characteristics of the device are determined by solving an eigenvalue problem alone. Response calculations are not necessary. Natural frequency and vibration mode analyses are important in the design stage when several different configurations are being considered.

Use of Eq. (18b) into Eq. (16) gives the average power harvested by the single subsystem device as

$$\langle P\rangle = \frac{\frac{1}{2}\beta\omega^8}{\left[(1-\omega^2)(\gamma-\alpha\omega^2)-(1+\zeta\beta)\omega^2\right]^2+\left[\beta\omega(1-\omega^2)+\zeta\omega(\gamma-\alpha\omega^2)\right]^2}. \quad (19)$$

The average power harvested calculated from Eq. (19) is shown by the dash-dotted (red) line in Fig. 4. There are two local maxima near the resonances of the device. The maximum average power harvested at the first resonance near $\omega = 0.828$ is $\langle P\rangle = 5.56$. This amplitude is significantly lower than that for the proof mass deflection and electric circuit charge. The maximum average power harvested at the second resonance near $\omega = 1.56$ is $\langle P\rangle = 25.7$. In contrast to that at the first resonance, the average power harvested here is substantially larger than both the deflection and charge. The average power harvested at the second resonance is greater than four times that at the first. For this device, the second mode performs better than the first for vibration energy harvesting applications.

The average power harvested for the case of forced excitation ($f = F_0 e^{j\omega t}$) and vanishing base excitation ($y \to 0$) is $\langle\tilde{P}\rangle = \langle P\rangle F_0^2/\omega^4$, where $\langle P\rangle$ is the average power harvested for the case of base excitation given in Eq. (19). Hence, the amplitude of average power harvested differs when the device is dynamically excited by applied forces compared to the case of base excitation, in contrast to what is reported in Ref. [25].

The changes in the single subsystem device's eigenvalues for varying nondimensional resistance β are shown in Fig. 5. For vanishing β the eigenvalues are complex-valued with small negative real parts due to the viscous damping in the device. The imaginary part of λ_1 (i.e., the natural frequency of the first mode) increases monotonically with increasing resistance for the entire range shown (Fig. 5(a)). The real part of λ_1 (which is related to the decay rate of the first mode) initially decreases with increasing resistance from $\beta = 0$. It reaches a local minimum near $\beta = 3.7$. For $\beta > 3.7$ the real part of λ_1 increases monotonically, but remains negative, with further increases in β. The imaginary part of λ_2 decreases monotonically with increasing β until near $\beta = 6.22$, where it vanishes. Above $\beta = 6.22$ the eigenvalues λ_2 and λ_{-2} are real-valued and negative, with one increasing and the other decreasing with further increases in resistance. This interaction is shown in a root locus diagram in Fig. 5(b). For increasing β between 0 and 6.22, the complex-valued λ_2 (λ_{-2}) has decreasing real part and decreasing (increasing) imaginary part. The eigenvalues λ_2 and λ_{-2} approach one another as the resistance increases toward $\beta = 6.22$. These eigenvalues coalesce on the real axis at $\beta = 6.22$. For increasing resistance above $\beta = 6.22$ they become real-valued and negative and remain that way for extremely high resistances (not shown). Because the resistance $\beta = 6.22$ separates complex-valued eigenvalues from purely real eigenvalues, we call it a critical resistance and denote it as β_{crit}. The critical resistance separates oscillatory free response ($\beta < \beta_{crit}$) from overdamped free response without oscillations ($\beta > \beta_{crit}$) for this mode.

Figure 6 shows a contour plot of the average power harvested at each resonance for varying nondimensional resistance β and excitation frequency ω. The natural frequency loci calculated from the eigenvalue problem in Eq. (11) are shown by dotted (black) lines. Although the natural frequencies do not change meaningfully for the range of resistances shown, the average power harvested varies substantially. The average power harvested has local maxima near the natural frequencies of the device. The resistance that maximizes the average power harvested differs between the two resonances. Near the first resonance (Fig. 6(a)) the maximum occurs near the nominal resistance (denoted by a dashed (red) vertical line). For the second resonance in Fig. 6(b), however, the maximum average power harvested occurs for a value of β near the viscous damping coefficient ζ (denoted by a dash-dotted (purple) vertical line). The exact electric circuit resistance that maximizes the average power harvested is determined by differentiation of Eq. (19)

with respect to β, equating that result to zero, and then solving for β. Closed-form solutions are difficult so the optimum resistance is determined numerically at each resonance. The optimum resistance at the first resonance near $\omega = 0.828$ is $\beta_{e1} = 0.0693$. The corresponding maximum power $\langle P \rangle = 5.87$. At the second resonance near $\omega = 1.56$ the optimum resistance is $\beta_{e2} = 0.0119$. The maximum average power harvested at this resistance is $\langle P \rangle = 73.7$. This is a 287% improvement in power harvested compared to the nominal resistance (Fig. 4). These results are verified by the contour plots shown in Fig. 6.

For single subsystem devices with purely resistive electric circuits [7, 17] and devices with adaptive circuits that include capacitance and inductance [25], the maximum power harvested is $\langle P \rangle = 1/8\zeta$ when the device is operated near resonance ($\omega = 1$) and $\beta = \zeta$. (Note that this expression is twice that given in Refs. [7, 17, 25] due to those works expressing the result in terms of the system's damping ratio, whereas here we use the nondimensional viscous damping coefficient.) For these devices the maximum average power harvested for $\zeta = 0.01$ is $\langle P \rangle = 12.5$. The single subsystem device proposed in this section harvests significantly more power than one with purely resistive circuits. We note that although the damping in these two cases is similar, the resistances differ substantially. The damping in devices with purely resistive circuits is inversely proportional to the resistance (see Eq. (6)). For single subsystem devices with inductance and capacitance the resistance is proportional to the damping (see Eq. (4)).

The sensitivity of the device's eigenvalues to changes in the nondimensional inductance is shown in Fig. 7(a). The nominal inductance is indicated by a dashed (red) vertical line. For increasing inductance from $\alpha = 1$, but below the nominal value, the natural frequency of the first mode (i.e., the imaginary part of λ_1) decreases slightly with increasing α. In contrast, the natural frequency of the second mode decreases rapidly in this range. These two natural frequencies interact with one another near the nominal inductance in a natural frequency veering region [44–47]. Before the veering region the trajectories of the two natural frequencies suggest that they will cross one another in the neighborhood of the nominal inductance. As the natural frequencies get closer to one another, however, they change course and veer away instead of intersecting. For increasing inductance above the nominal value the natural frequency of the first mode decreases substantially and that for the second mode decreases only slightly. The real part of λ_1 increases monotonically, but remains negative, for the entire range of inductances shown. The real part of λ_2 increases rapidly for increasing inductance from $\alpha = 1$. At higher inductances above the nominal value it becomes much less sensitive to increasing inductance.

Figure 7(b) shows the sensitivity of the device's eigenvalues to changes in γ, which is inversely proportional to the capacitance in the electric circuit. The natural frequencies of the device increase with increasing γ. The two natural frequencies have a veering away region near the nominal value of γ (denoted by a dashed (red) vertical line). This veering region is wider than that seen in Fig. 7(a) when the nondimensional inductance α is varied. The real parts of the eigenvalues remain negative for the entire range shown. They are only sensitive to γ in the region between 0.1 and 10. The real part of λ_1 increases monotonically with increasing γ in this range. In contrast, the real part of λ_2 decreases monotonically with increasing γ. Outside of the region $0.1 < \gamma < 10$, the real parts of the eigenvalues do not change meaningfully with changes in γ.

The results in Figs. 5 and 7 show that the electric circuit parameters significantly affect the vibration of the energy harvesting device. These parameters, like those for the proof mass and elastic structure, could be used to tune the device's dynamics for optimal performance.

3.2 Double subsystem device

This section investigates a device with two subsystems ($N = 2$), which powers two separate electrical loads. The first subsystem has $m_1 = 1\ kg$, $c_1 = 5\ Ns/m$, $k_1 = 1\ kN/mm$, $L_1 = 1\ mH$, $R_1 = 0.1\ \Omega$, $C_1 = 0.3\ mF$, and $\kappa_1 = 30\ N/A$. The second subsystem has $m_2 = 0.5\ kg$, $c_2 = 5\ Ns/m$, $k_2 = 0.2\ kN/mm$, $L_2 = 2\ mH$, $R_2 = 0.1\ \Omega$, $C_2 = 0.15\ mF$, and $\kappa_2 = 30\ N/A$. The device's eigenvalues and eigenvectors are numerically determined from the eigenvalue problem in Eq. (11) using these parameters. This device has four pairs of complex-conjugate eigenvalues: $\lambda_1 = \overline{\lambda}_{-1} = -0.00300 + j0.510$, $\lambda_2 = \overline{\lambda}_{-2} = -0.00743 + j0.889$, $\lambda_3 = \overline{\lambda}_{-3} = -0.0401 + j1.96$, and $\lambda_4 = \overline{\lambda}_{-4} = -0.0344 + j2.37$. Because this device has complex-valued eigenvalues with negative real parts, its corresponding single-mode free response will have decaying oscillations, like that shown in Fig. 2 for the single subsystem device. The complex-valued eigenvectors of the double subsystem device are shown in Fig. 8 by the magnitudes and phases of each coordinate. All the vibration modes for this device are electromechanically coupled, although the strength of the coupling varies between the modes. The first eigenvector $\boldsymbol{\chi}_1$ (Fig. 8(a)) has weak electromechanical coupling, as seen by the large differences in amplitude between the deflections and charges. This mode is dominated by the deflection of the second proof mass $|X_2|$. There is meaningful electromechanical coupling in $\boldsymbol{\chi}_2$ (Fig. 8(b)), although this mode is dominated by the deflection of the first proof mass $|X_1|$. The eigenvectors $\boldsymbol{\chi}_3$ (Fig. 8(c)) and $\boldsymbol{\chi}_4$ (Fig. 8(d)) have strong electromechanical coupling. The magnitude of the first charge $|Q_1|$ is meaningfully larger than that for the other coordinates in $\boldsymbol{\chi}_3$. This mode will likely be a good candidate for energy harvesting applications, in particular, for providing power to the resistance in the first subsystem. The components of $\boldsymbol{\chi}_4$ have nearly identical magnitudes. This mode could potentially harvest large amounts of power for each resistance simultaneously.

There are specific phase differences between the coordinates of $\boldsymbol{\chi}_{1-4}$ in Fig. 8. The deflections $X_{1,2}$ are always nearly in-phase (Figs. 8(a,c)) or nearly π radians out-of-phase (Figs. 8(b,d)). Similarly, the charges $Q_{1,2}$ are always nearly in-phase (Figs. 8(a,c)) or nearly π radians out-of-phase (Figs. 8(b,d)). The electric circuit charges either lead or lag the proof mass deflections by nearly $\pi/2$ radians. This phase difference also occurs between charges and deflections in Figs. 2 and 3 for the single subsystem device.

Figure 9 shows the dynamic response for a wide range of excitation frequencies that include the device's four resonances. The device is dynamically excited by nondimensional sinusoidal base motion $y(t) = \cos \omega t$. The applied dynamic forces $f_{1,2}$ vanish. The results in Fig. 9 have been validated by numerical integration of Eq. (8) (not shown). The four resonant frequencies of the device seen in Fig. 9 occur near its natural frequencies, which are obtained from the imaginary parts of the eigenvalues. At the first resonance near $\omega = 0.510$ the device has large amplitude deflections of the proof masses, in particular, $|X_2|$. The response at the second resonance near $\omega = 0.889$, like that at the first, has large amplitude deflections of the proof masses. At this frequency $|X_1|$ has the largest amplitude (Fig. 9(a)). The response at the third resonance near $\omega = 1.96$ has significant vibration in all coordinates; the charge in the first circuit has the largest amplitude vibration. At the fourth resonance ($\omega \approx 2.37$) the deflections $|X_{1,2}|$ and charges $|Q_{1,2}|$ have similar amplitudes. The features of the device's dynamic response at resonance agree with those of the corresponding vibration modes in Fig. 8. The agreement between the eigenvalue problem results and response calculations for the double subsystem device further demonstrates the utility of solving eigenvalue problems for electromagnetic vibration energy harvesters.

The average power harvested by the double subsystem device is shown by the dash-dotted (red) lines in Fig. 9. The maximum average power harvested by the resistance in the first subsystem is $\langle P_1 \rangle = 13.1$, which occurs at the third resonance (near $\omega = 1.96$ in Fig. 9(a)). The maximum average power harvested by the resistance in the second subsystem at this frequency is $\langle P_2 \rangle = 4.09$ (Fig. 9(b)), which is nearly one-third of that for the resistance in the first subsystem. At the fourth resonance ($\omega \approx 2.37$) the maxima are $\langle P_1 \rangle = 12.5$ (Fig. 9(a)) and $\langle P_2 \rangle = 10.5$ (Fig. 9(b)). At the second resonance near $\omega = 0.889$ the maximum average power harvested is $\langle P_1 \rangle = 3.85$ and $\langle P_2 \rangle = 1.31$. The sharpness of these resonances, in addition to their small amplitudes, would make energy harvesting at this frequency challenging. The first resonance near $\omega = 0.510$ has negligible amplitudes of average power harvested, as suggested by the weak electromechanical coupling in $\boldsymbol{\chi}_1$ (Fig. 8(a)).

The results from Fig. 9 suggest that this device has two modes where large amounts of energy can be harvested. The device's third resonance is suited to applications where the two electrical loads (i.e., the resistances in each subsystem) require different amounts of electrical power. Operation of the double subsystem device near the fourth resonance provides similar amounts of electrical power to both resistances simultaneously. The remaining two modes are not likely suitable for energy harvesting applications. Devices with two subsystems and two resonances where large amounts of energy are harvested are suited to applications that have two operating conditions.

A contour plot of the average power harvested by the double subsystem device for varying nondimensional resistance β_1 and excitation frequency ω is shown in Fig. 10 for excitation frequencies that include the third and fourth resonances. The device's natural frequencies (the dotted (black) lines calculated from Eq. (11)) are not sensitive to changes in β_1 below the nominal value (denoted by a dashed (red) vertical line). For resistances above its nominal value the natural frequencies vary substantially with β_1. The ω_3 locus is particularly sensitive to resistance above $\beta_1 = 1$. This locus vanishes at $\beta_{1crit} = 4.45$ (not shown). Interestingly, no other natural frequencies vanish as β_1 increases, even for extremely large β_1. The maximum average power harvested by the first resistance is $\langle P_1 \rangle = 17.9$, which occurs for $\beta_1 = 0.0363$ at the third resonance (near $\omega = 1.96$ in Fig. 10(a)). Another local maximum occurs for $\beta_1 = 0.120$ at the fourth resonance ($\omega \approx 2.37$). Here the maximum average power harvested is $\langle P_1 \rangle = 12.4$. As seen in Fig. 10(b), the average power harvested by the second resistance increases monotonically with decreasing β_1. This makes sense intuitively because decreasing β_1 decreases the total damping in the device, which results in larger amplitude vibrations and larger amounts of power harvested by the resistance in the second subsystem. At $\beta_1 = 0.001$ (the smallest value shown) the maximum average powers harvested at the third and fourth resonances are $\langle P_2 \rangle = 66.0$ and $\langle P_2 \rangle = 37.8$, respectively. The power harvested by both resistances decreases with increasing β_1 from its nominal value.

Figure 11 shows that the average power harvested by the double subsystem device differs substantially with changes in γ_1. For all values of γ_1 shown large amplitudes occur near the natural frequency loci (dotted (black) lines) calculated from Eq. (11). The average power harvested near $\omega_{1,2}$ is small for all γ_1 shown. Two veering away regions (denoted as "VA") occur. The ω_1 and ω_2 loci veer away near $\gamma_1 = 0.800$. A region of veering away occurs between ω_3 and ω_4 near the nominal value of γ_1.

Figure 12 shows the difference in average power harvested at the third and fourth resonances for two configurations of the double subsystem device that each power only a single resistance. When the device is operated near ω_3 the device that powers only the second resistance (solid (black) line) harvests substantially more power than the identical device that powers only the first resistance (dashed (red) line). Near ω_4 similar amounts of power are harvested by each configuration. The power harvested near the first two resonances (not shown) is negligible for both device configurations.

4 Conclusions

By casting the eigenvalue problem for electromagnetic vibration energy harvesters into matrix operator form the qualitative properties of their vibration are revealed. These devices generally have complex-valued eigenvalues and eigenvectors because of electromechanical coupling, viscous mechanical damping, and damping associated with the power dissipated by the resistances in the electric circuits. The imaginary parts of the eigenvalues are the device's natural frequencies, where large amplitude vibrations occur in forced response. The eigenvalues have negative real parts, which physically represent exponentially decaying oscillations in single-mode free response. The complex-valued components of the eigenvectors physically represent the amplitudes and phases of the device's deflections and charges in single-mode free or forced vibration.

Devices with a single subsystem (i.e., a single proof mass, elastic structure, electromagnetic generator, and energy harvesting circuit) have two resonances. Because the maximum average power harvested at each resonance differs substantially, only one of the device's two vibration modes is suited to vibration energy harvesting applications. The maximum average power harvested occurs for resistances slightly above the viscous damping coefficients. Double subsystem devices can simultaneously power two separate electrical loads. These devices have four resonances. Only two of these four modes are suitable for vibration energy harvesting applications. In one mode the average power harvested by each resistance is meaningfully different. The other mode has nearly identical amounts of average power harvested by each resistance. The eigenvectors with strong electromechanical coupling, as determined by the relative magnitudes of their vibration coordinates, generally produce large amplitudes of average power harvested.

The device's eigenvalues, dynamic response, and average power harvested are sensitive to the inductance, resistance, and capacitance in the electric circuit. The device's natural frequencies do not change significantly with changes in resistance in the vicinity of the maximum power harvested. At higher resistances, however, the natural frequencies are highly sensitive to changes in resistance. Overdamped vibration behavior is possible for sufficiently large resistances. Regions of natural frequency veering occur as the inductances and capacitances vary due to electromechanical coupling in the device.

Acknowledgments

We gratefully acknowledge the Advanced Coal and Energy Research Center at Southern Illinois University Carbondale for their support of this research.

References

[1] Anton, S. R., and Sodano, H. A., 2007. "A review of power harvesting using piezoelectric materials (2003-2006)". *Smart Materials and Structures,* **16**(3), June, p. R1.

[2] Harne, R. L., and Wang, K. W., 2013. "A review of the recent research on vibration energy harvesting via bistable systems". *Smart Materials and Structures,* **22**(2), Feb., p. 023001.

[3] Calio, R., Rongala, U. B., Camboni, D., Milazzo, M., Stefanini, C., de Petris, G., and Oddo, C. M., 2014. "Piezoelectric Energy Harvesting Solutions". *Sensors,* **14**(3), Mar., pp. 4755–4790.

[4] Daqaq, M. F., Masana, R., Erturk, A., and Quinn, D. D., 2014. "On the Role of Nonlinearities in Vibratory Energy Harvesting: A Critical Review and Discussion". *Applied Mechanics Reviews,* **66**(4), May, p. 040801.

[5] Williams, C. B., and Yates, R. B., 1996. "Analysis of a micro-electric generator for microsystems". *Sensors and Actuators A: Physical,* **52**(13), Mar., pp. 8–11.

[6] El-hami, M., Glynne-Jones, P., White, N. M., Hill, M., Beeby, S., James, E., Brown, A. D., and Ross, J. N., 2001. "Design and fabrication of a new vibration-based electromechanical power generator". *Sensors and Actuators A: Physical,* **92**(13), Aug., pp. 335–342.

[7] Stephen, N. G., 2006. "On energy harvesting from ambient vibration". *Journal of Sound and Vibration,* **293**(12), May, pp. 409–425.

[8] Mann, B. P., and Sims, N. D., 2010. "On the performance and resonant frequency of electromagnetic induction energy harvesters". *Journal of Sound and Vibration,* **329**(9), Apr., pp. 1348–1361.

[9] Mann, B. P., and Sims, N. D., 2009. "Energy harvesting from the nonlinear oscillations of magnetic levitation". *Journal of Sound and Vibration,* **319**(12), Jan., pp. 515–530.

[10] Yang, B., Lee, C., Xiang, W., Xie, J., He, J. H., Kotlanka, R. K., Low, S. P., and Hanhua Feng, 2009. "Electromagnetic energy harvesting from vibrations of multiple frequencies". *Journal of Micromechanics and Microengineering,* **19**(3), p. 035001.

[11] Mann, B. P., and Owens, B. A., 2010. "Investigations of a nonlinear energy harvester with a bistable potential well". *Journal of Sound and Vibration,* **329**(9), Apr., pp. 1215–1226.

[12] Trimble, A. Z., Lang, J. H., Pabon, J., and Slocum, A., 2010. "A Device for Harvesting Energy From Rotational Vibrations". *Journal of Mechanical Design,* **132**(9), Aug., p. 091001.

[13] Cammarano, A., Burrow, S. G., Barton, D. A. W., Carrella, A., and Clare, L. R., 2010. "Tuning a resonant energy harvester using a generalized electrical load". *Smart Materials and Structures,* **19**(5), p. 055003.

[14] Zuo, L., Scully, B., Shestani, J., and Zhou, Y., 2010. "Design and characterization of an electromagnetic energy harvester for vehicle suspensions". *Smart Materials and Structures,* **19**(4), p. 045003.

[15] Elvin, N. G., and Elvin, A. A., 2011. "An experimentally validated electromagnetic energy harvester". *Journal of Sound and Vibration,* **330**(10), May, pp. 2314–2324.

[16] Daqaq, M. F., 2011. "Transduction of a bistable inductive generator driven by white and exponentially correlated Gaussian noise". *Journal of Sound and Vibration,* **330**(11), May, pp. 2554–2564.

[17] Tang, X., and Zuo, L., 2011. "Enhanced vibration energy harvesting using dual-mass systems". *Journal of Sound and Vibration,* **330**(21), Oct., pp. 5199–5209.

[18] Arafa, M. H., 2012. "Multi-Modal Vibration Energy Harvesting Using a Trapezoidal Plate". *Journal of Vibration and Acoustics,* **134**(4), May, p. 041010.

[19] Green, P. L., Worden, K., Atallah, K., and Sims, N. D., 2012. "The benefits of Duffing-type nonlinearities and electrical optimisation of a mono-stable energy harvester under white Gaussian excitations". *Journal of Sound and Vibration,* **331**(20), Sept., pp. 4504–4517.

[20] Green, P. L., Worden, K., and Sims, N. D., 2013. "On the identification and modelling of friction in a randomly excited energy harvester". *Journal of Sound and Vibration,* **332**(19), Sept., pp. 4696–4708.

[21] Tang, X., and Zuo, L., 2012. "Vibration energy harvesting from random force and motion excitations". *Smart Materials and Structures,* **21**(7), p. 075025.

[22] Harne, R. L., 2013. "Modeling and analysis of distributed electromagnetic oscillators for broadband vibration attenuation and concurrent energy harvesting". *Applied Mathematical Modelling,* **37**(6), Mar., pp. 4360–4370.

[23] He, Q., and Daqaq, M. F., 2014. "Influence of potential function asymmetries on the performance of nonlinear energy harvesters under white noise". *Journal of Sound and Vibration,* **333**(15), July, pp. 3479–3489.

[24] Gonzalez-Buelga, A., Clare, L. R., Neild, S. A., Burrow, S. G., and Inman, D. J., 2015. “An electromagnetic vibration absorber with harvesting and tuning capabilities”. *Structural Control and Health Monitoring,* **22**(11), Nov., pp. 1359–1372.

[25] Caruso, G., 2015. “Broadband Energy Harvesting From Vibrations Using Magnetic Transduction”. *Journal of Vibration and Acoustics,* **137**(6), Oct., p. 064503.

[26] Halim, M. A., Cho, H., and Park, J. Y., 2015. “Design and experiment of a human-limb driven, frequency up-converted electromagnetic energy harvester”. *Energy Conversion and Management,* **106**, Dec., pp. 393–404.

[27] Palagummi, S., Zou, J., and Yuan, F. G., 2015. “A Horizontal Diamagnetic Levitation Based Low Frequency Vibration Energy Harvester”. *Journal of Vibration and Acoustics,* **137**(6), Dec., pp. 061004–061004.

[28] Tang, X., Liu, Y., Cui, W., and Zuo, L., 2015. “Analytical Solutions to H2 and H Optimizations of Resonant Shunted Electromagnetic Tuned Mass Damper and Vibration Energy Harvester”. *Journal of Vibration and Acoustics,* **138**(1), Nov., pp. 011018–011018.

[29] Sodano, H. A., Park, G., and Inman, D. J., 2004. “Estimation of Electric Charge Output for Piezoelectric Energy Harvesting”. *Strain,* **40**(2), May, pp. 49–58.

[30] duToit, N. E., Wardle, B. L., and Kim, S.-G., 2005. “Design Considerations for Mems-Scale Piezoelectric Mechanical Vibration Energy Harvesters”. *Integrated Ferroelectrics,* **71**(1), July, pp. 121–160.

[31] Renno, J. M., Daqaq, M. F., and Inman, D. J., 2009. “On the optimal energy harvesting from a vibration source”. *Journal of Sound and Vibration,* **320**(12), Feb., pp. 386–405.

[32] Adhikari, S., Friswell, M. I., and Inman, D. J., 2009. “Piezoelectric energy harvesting from broadband random vibrations”. *Smart Materials and Structures,* **18**(11), p. 115005.

[33] Seuaciuc-Osrio, T., and Daqaq, M. F., 2010. “Energy harvesting under excitations of time-varying frequency”. *Journal of Sound and Vibration,* **329**(13), June, pp. 2497–2515.

[34] duToit, N. E., and Wardle, B. L., 2007. “Experimental Verification of Models for Microfabricated Piezoelectric Vibration Energy Harvesters”. *AIAA Journal,* **45**(5), pp. 1126–1137.

[35] Erturk, A., Bilgen, O., and Inman, D. J., 2008. “Power generation and shunt damping performance of a single crystal lead magnesium niobate-lead zirconate titanate unimorph: Analysis and experiment”. *Applied Physics Letters,* **93**(22), Dec., p. 224102.

[36] Erturk, A., and Inman, D. J., 2008. "A Distributed Parameter Electromechanical Model for Cantilevered Piezoelectric Energy Harvesters". *Journal of Vibration and Acoustics,* **130**(4), June, p. 041002.

[37] Erturk, A., and Inman, D. J., 2009. "An experimentally validated bimorph cantilever model for piezoelectric energy harvesting from base excitations". *Smart Materials and Structures,* **18**(2), p. 025009.

[38] Masana, R., and Daqaq, M. F., 2010. "Electromechanical Modeling and Nonlinear Analysis of Axially Loaded Energy Harvesters". *Journal of Vibration and Acoustics,* **133**(1), Dec., pp. 011007–011007.

[39] Cottone, F., Gammaitoni, L., Vocca, H., Ferrari, M., and Ferrari, V., 2012. "Piezoelectric buckled beams for random vibration energy harvesting". *Smart Materials and Structures,* **21**(3), Mar., p. 035021.

[40] Harne, R. L., and Wang, K. W., 2015. "Axial Suspension Compliance and Compression for Enhancing Performance of a Nonlinear Vibration Energy Harvesting Beam System". *Journal of Vibration and Acoustics,* **138**(1), Oct., p. 011004.

[41] Ou, Q., Chen, X., Gutschmidt, S., Wood, A., Leigh, N., and Arrieta, A. F., 2012. "An experimentally validated double-mass piezoelectric cantilever model for broadband vibrationbased energy harvesting". *Journal of Intelligent Material Systems and Structures,* **23**(2), Jan., pp. 117–126.

[42] Tang, L., and Yang, Y., 2012. "A multiple-degree-of-freedom piezoelectric energy harvesting model". *Journal of Intelligent Material Systems and Structures,* **23**(14), Sept., pp. 1631–1647.

[43] Xiao, H., Wang, X., and John, S., 2016. "A multi-degree of freedom piezoelectric vibration energy harvester with piezoelectric elements inserted between two nearby oscillators". *Mechanical Systems and Signal Processing,* **6869**, Feb., pp. 138–154.

[44] Leissa, A. W., 1974. "On a curve veering aberration". *Zeitschrift fr angewandte Mathematik und Physik ZAMP,* **25**(1), Jan., pp. 99–111.

[45] Kuttler, J. R., and Sigillito, V. G., 1981. "On curve veering". *Journal of Sound and Vibration,* **75**(4), Apr., pp. 585–588.

[46] Perkins, N. C., and Mote, C. D., 1986. "Comments on curve veering in eigenvalue problems". *Journal of Sound and Vibration,* **106**(3), May, pp. 451–463.

[47] Pierre, C., 1988. “Mode localization and eigenvalue loci veering phenomena in disordered structures”. *Journal of Sound and Vibration,* **126**(3), Nov., pp. 485–502.

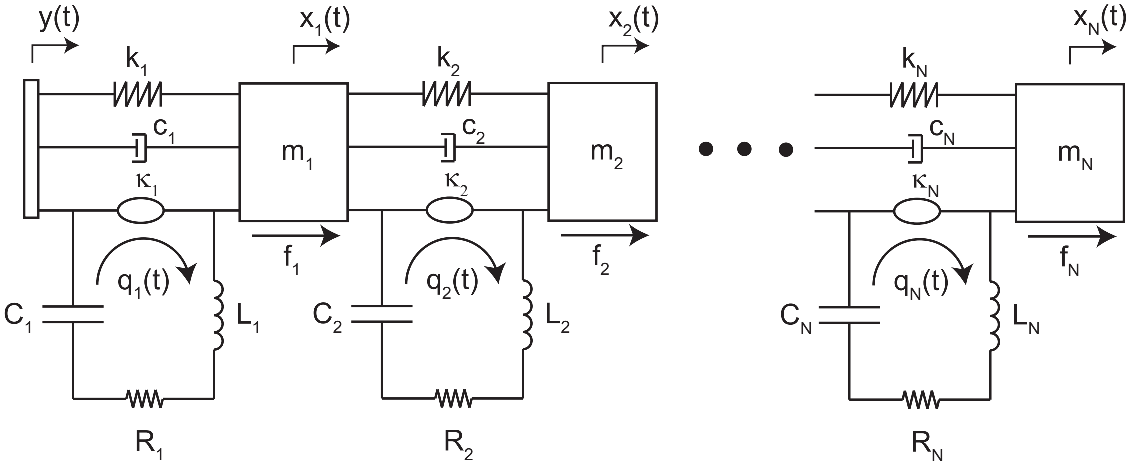

Figure 1: Schematic of a system of electromagnetic vibration energy harvesting devices.

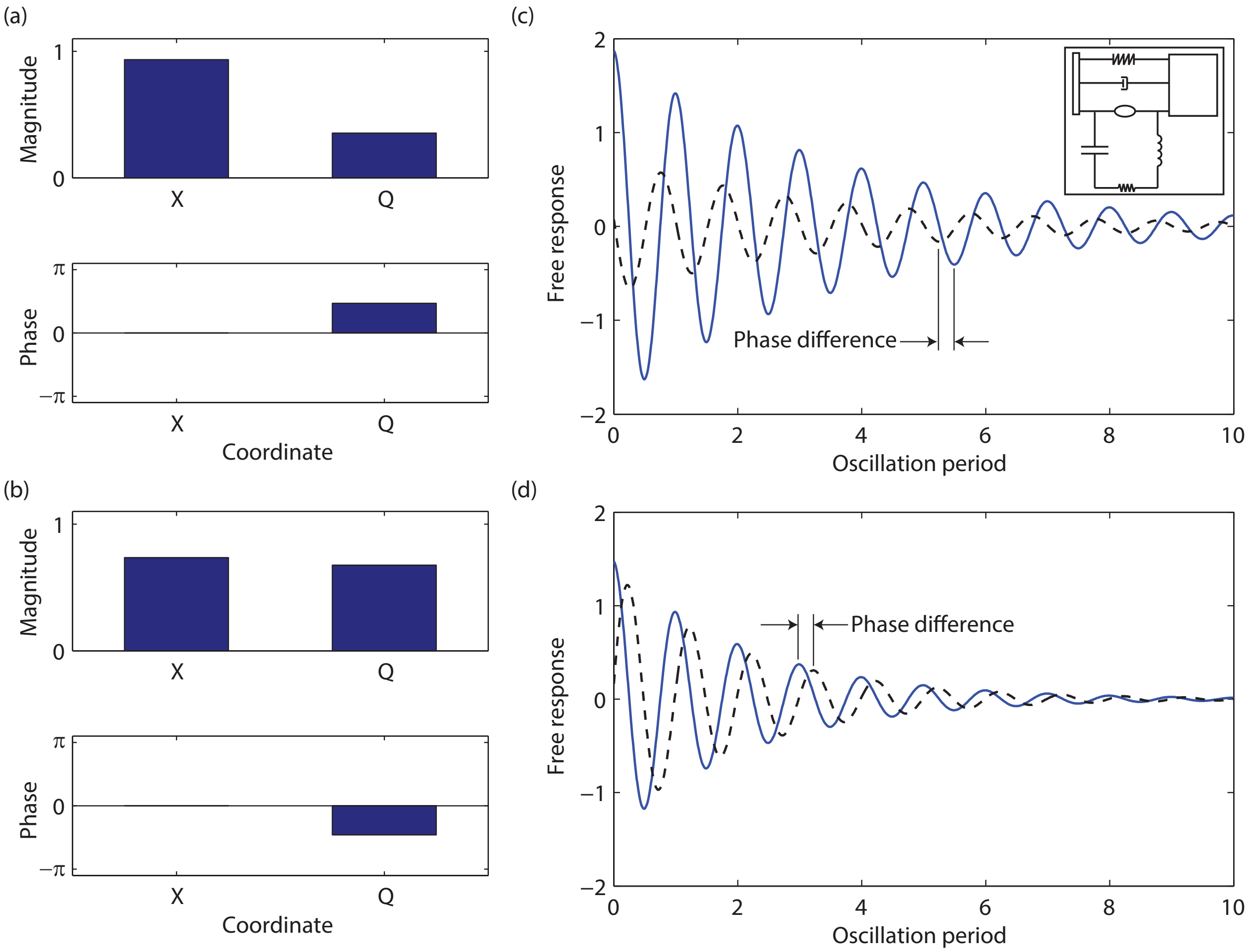

Figure 2: Single subsystem vibration energy harvester eigenvectors (a) $\boldsymbol{\chi}_1$ and (b) $\boldsymbol{\chi}_2$. Single-mode free response of (c) mode 1 ($\boldsymbol{\chi}_1$) and (d) mode 2 ($\boldsymbol{\chi}_2$). The solid (blue) and dashed (black) lines in (c,d) are the deflection (x) of the proof mass and charge (q) in the electric circuit, respectively.

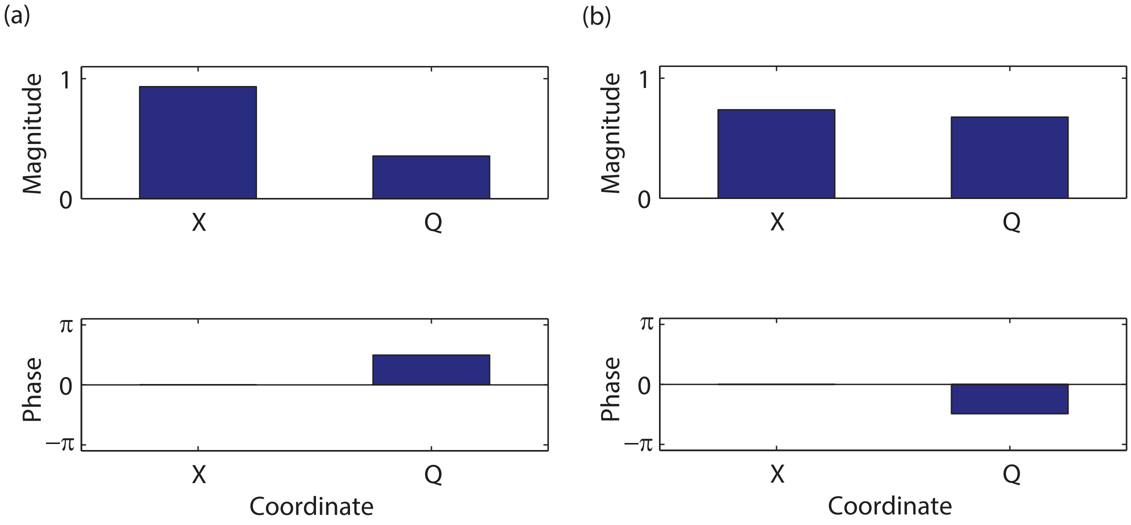

Figure 3: Magnitudes and phases of the complex-valued components of the single subsystem device eigenvectors. (a) $\boldsymbol{\chi}_1$ ($\lambda_1 = -0.00731 + j0.828$) and (b) $\boldsymbol{\chi}_2$ ($\lambda_2 = -0.0227 + j1.56$).

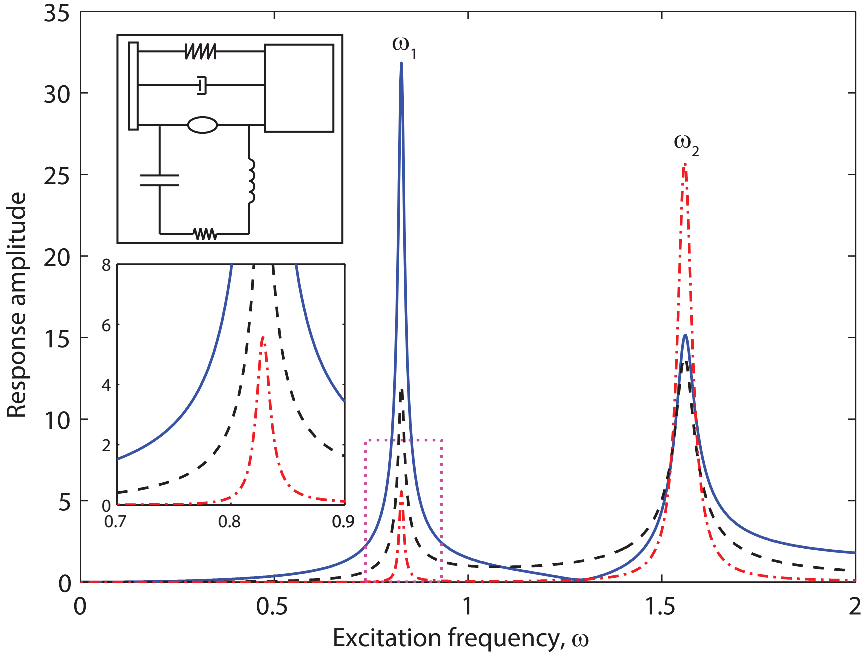

Figure 4: Single subsystem device dynamic response and average power harvested. The solid (blue), dashed (black), and dash-dotted (red) lines are the proof mass deflection, electric circuit charge, and average power harvested, respectively.

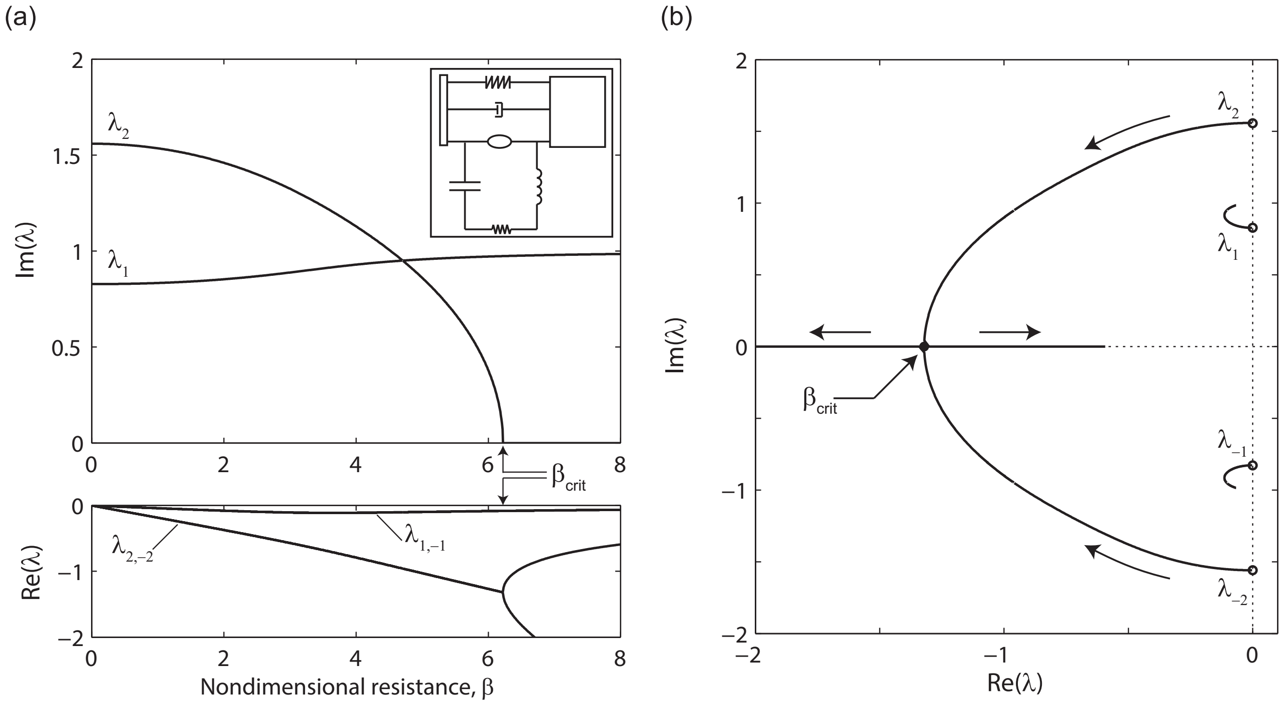

Figure 5: Single subsystem device (a) eigenvalue loci and (b) root locus diagram for varying nondimensional resistance β.

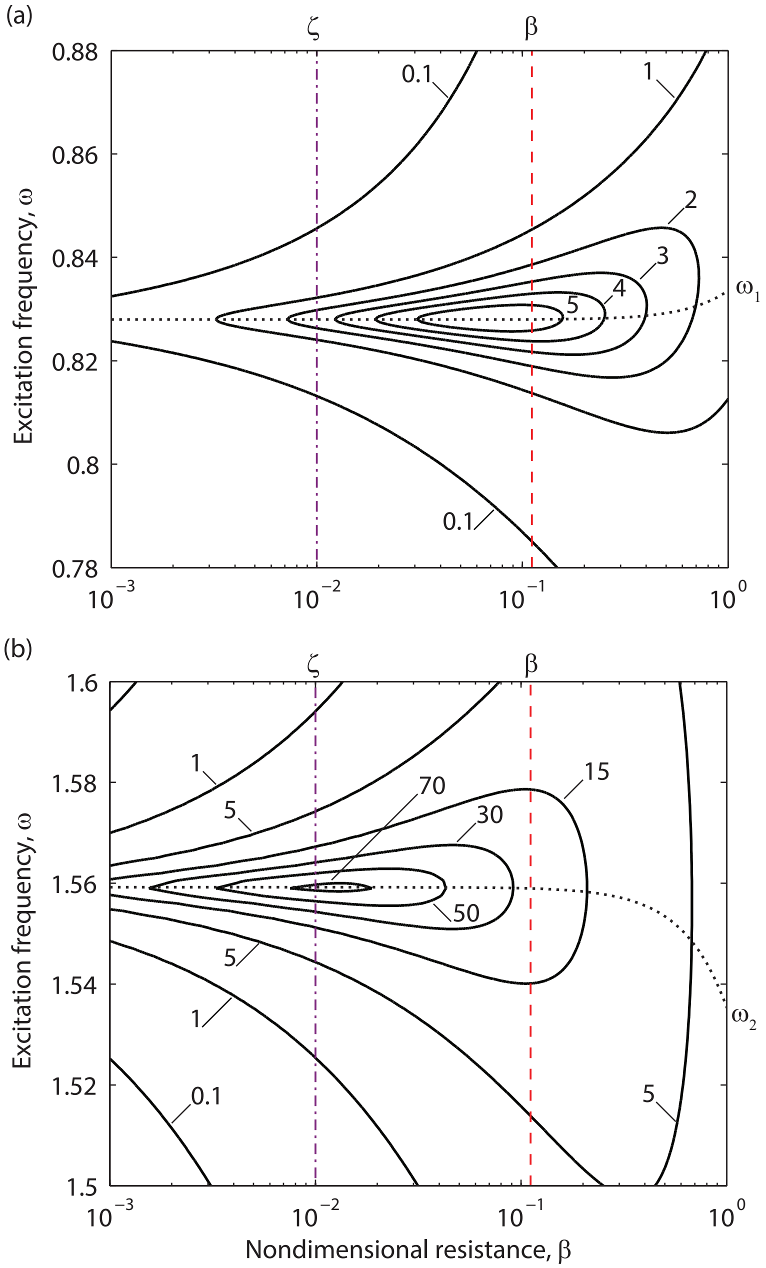

Figure 6: Contour plot of the average power harvested $\langle P \rangle$ by a single subsystem device for varying resistance β and base excitation frequency ω near the (a) first and (b) second resonances of the device. The dotted (black) lines are the natural frequency loci.

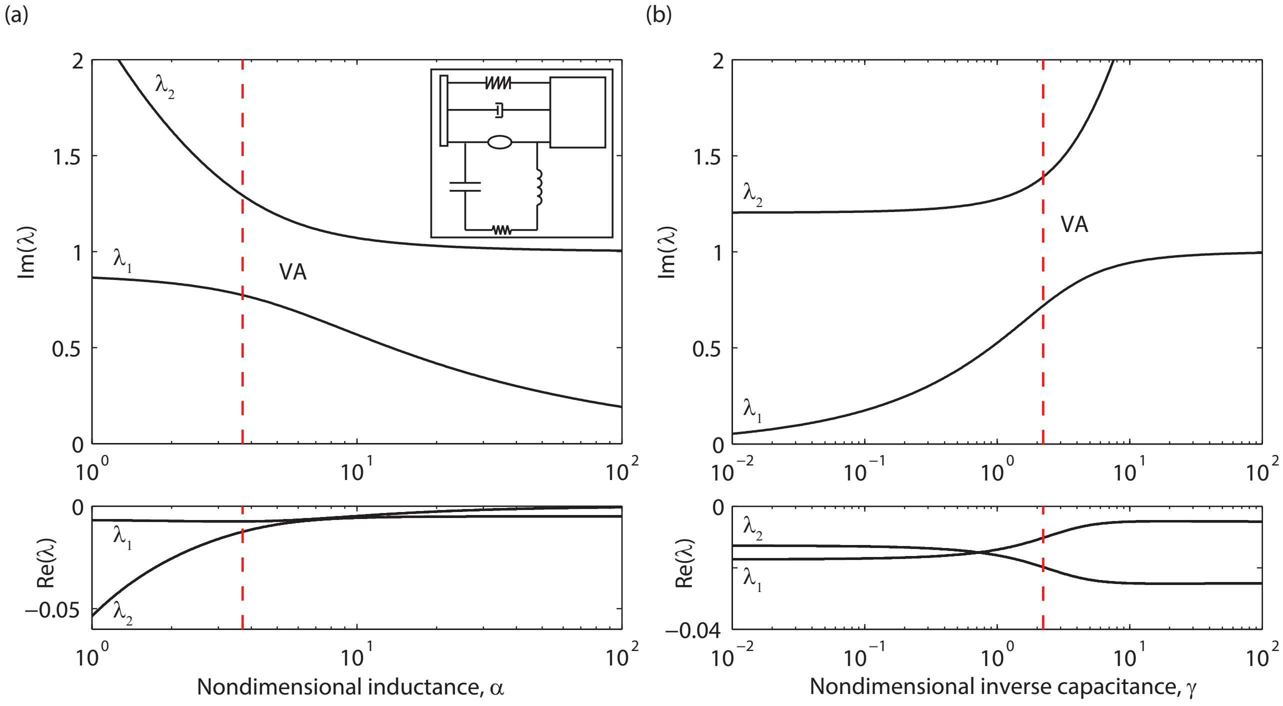

Figure 7: Single subsystem device eigenvalue loci for varying nondimensional (a) inductance and (b) inverse of capacitance. The dashed (red) vertical lines denote the nominal parameter values. "VA" denotes the veering away of two natural frequency loci.

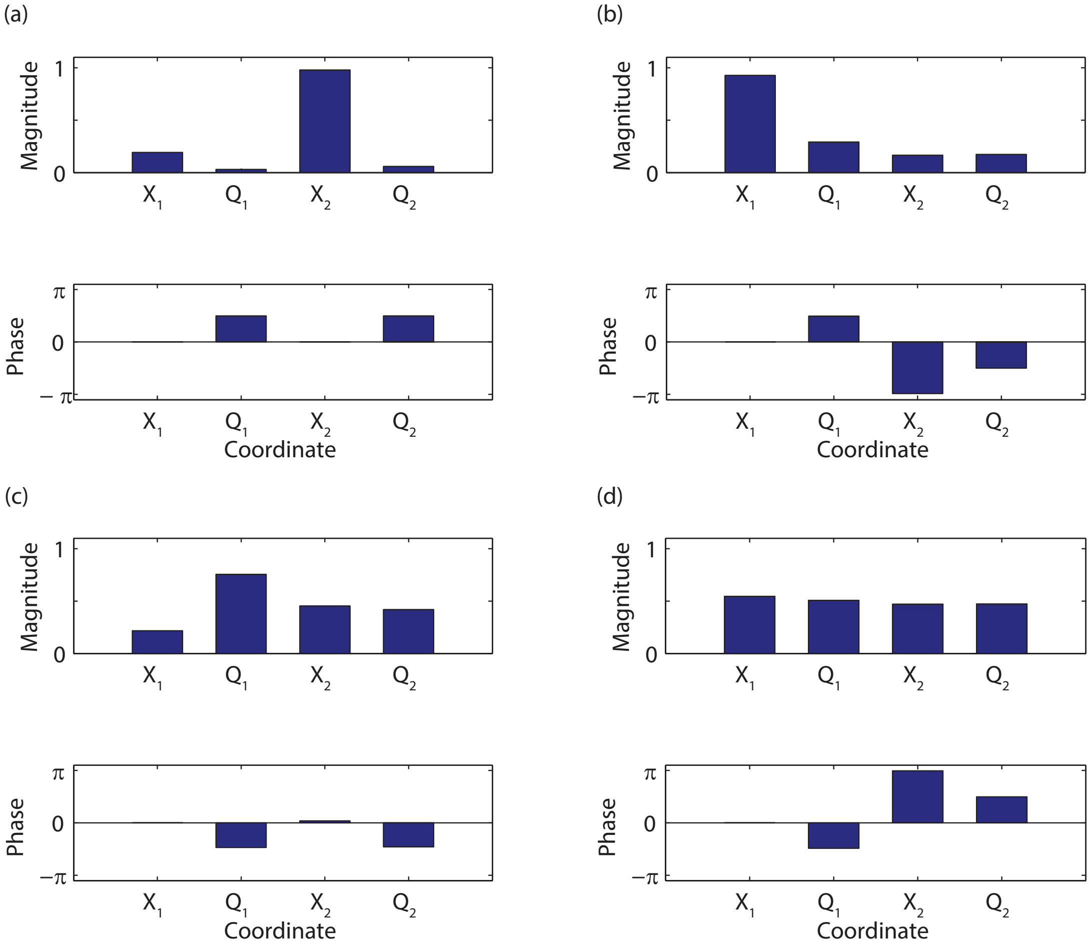

Figure 8: Magnitudes and phases of the complex-valued components of the double subsystem device eigenvectors. (a) $\boldsymbol{\chi}_1$ ($\lambda_1 = -0.00300 + j0.510$), (b) $\boldsymbol{\chi}_2$ ($\lambda_2 = -0.00743 + j0.889$), (c) $\boldsymbol{\chi}_3$ ($\lambda_3 = -0.0401 + j1.96$), and (d) $\boldsymbol{\chi}_4$ ($\lambda_4 = -0.0344 + j2.37$).

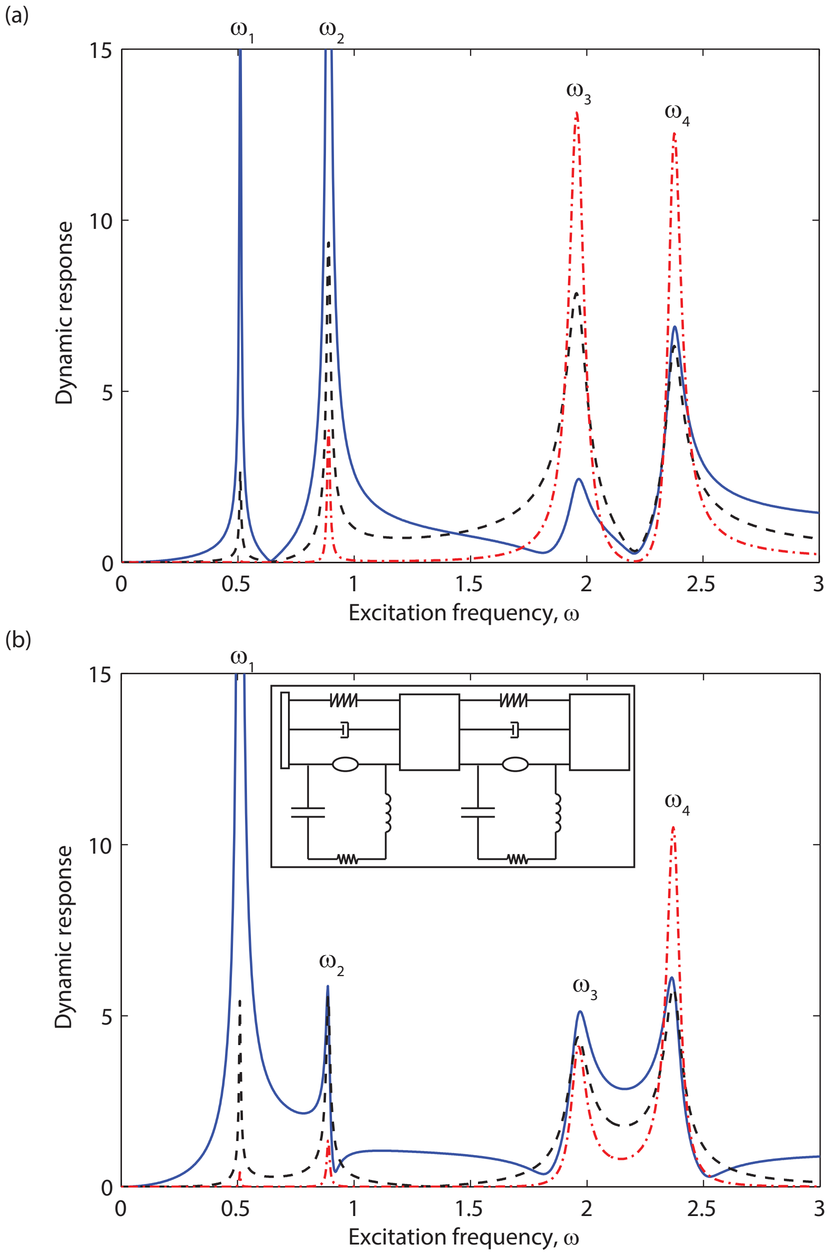

Figure 9: Double subsystem device dynamic response and average power harvested in the (a) first and (b) second subsystems. The proof mass deflections, electric circuit charges, and average powers harvested are shown by solid (blue), dashed (black), and dash-dotted (red) lines, respectively.

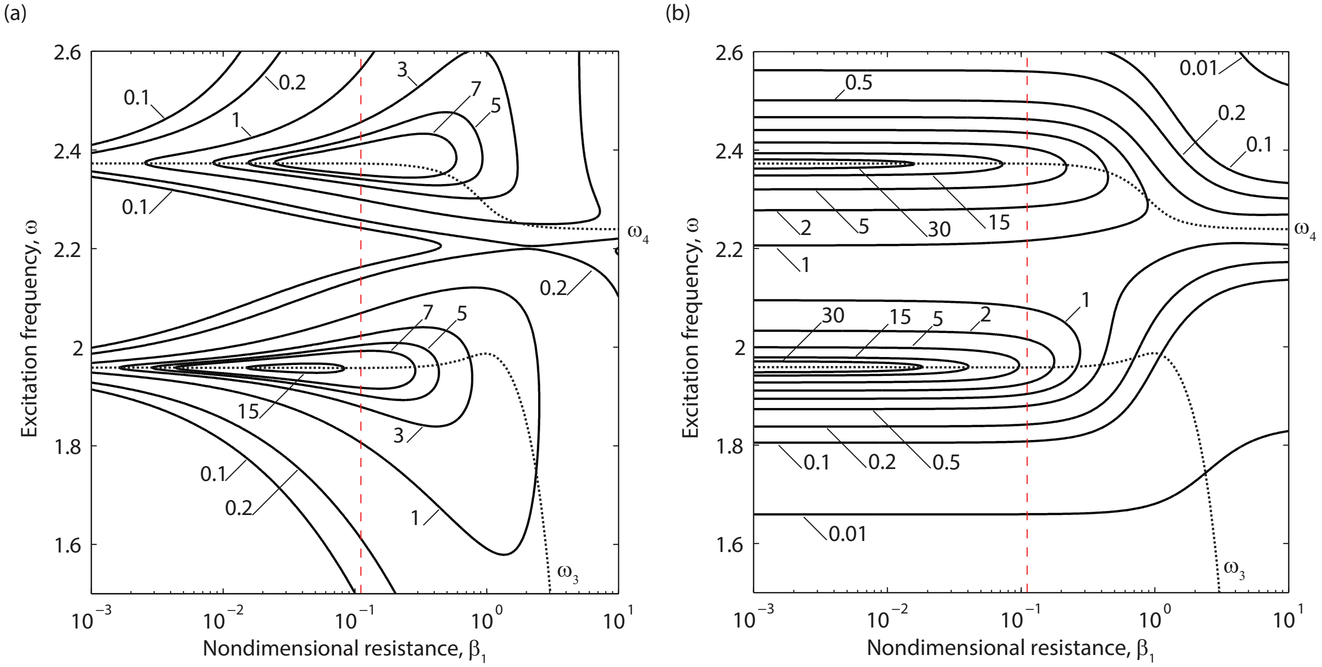

Figure 10: Contour plots of the average power harvested (a) $\langle P_1 \rangle$ and (b) $\langle P_2 \rangle$ by the double subsystem device for varying nondimensional resistance β_1 and excitation frequency ω. The dashed (red) vertical lines denote the nominal resistance. The dotted lines are the natural frequency loci.

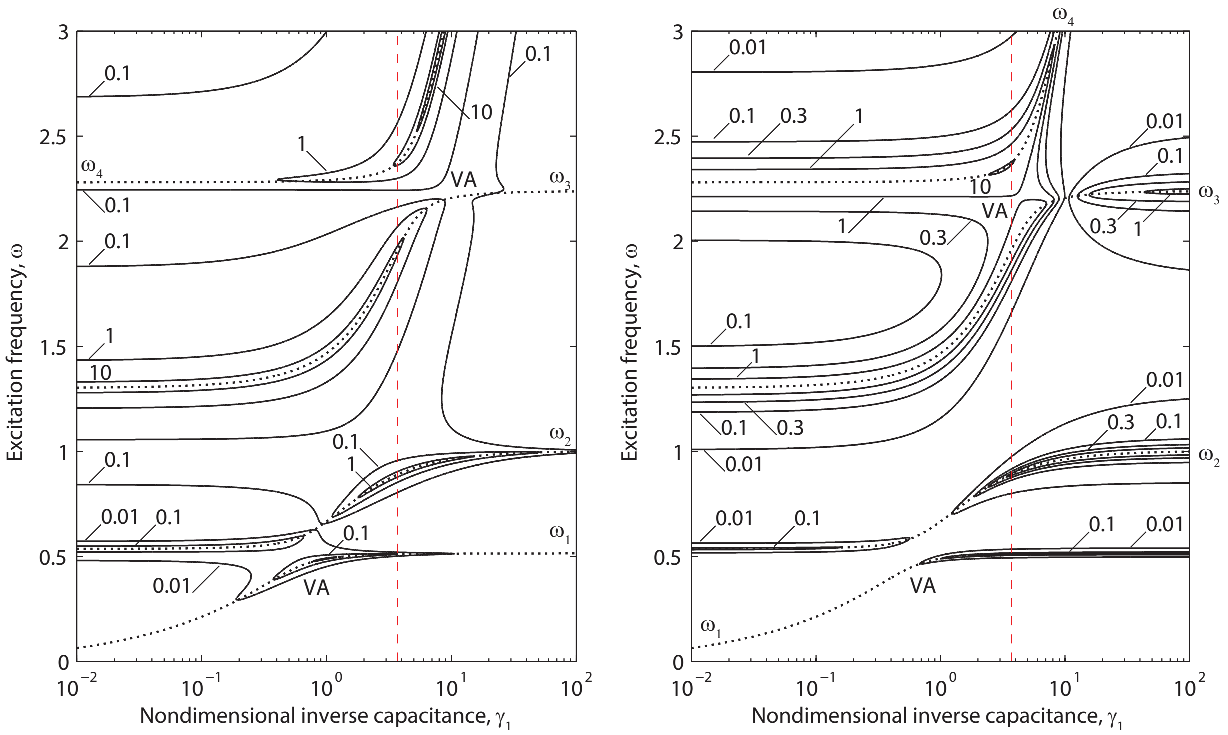

Figure 11: Contour plots of the average power harvested (a) $\langle P_1 \rangle$ and (b) $\langle P_2 \rangle$ by the double subsystem device for varying nondimensional inverse capacitance γ_1 and excitation frequency ω. The dashed (red) vertical lines denote the nominal inverse capacitance. The dotted (black) lines are the natural frequency loci.

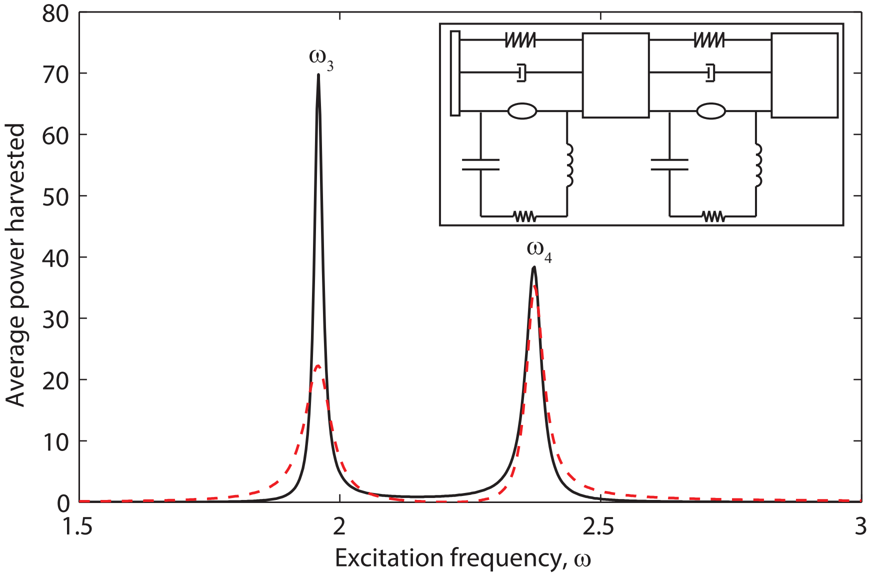

Figure 12: Average power harvested by the double subsystem device for varying excitation frequency near the third and fourth resonances. The solid (black) line is the power harvested by the second resistance $\langle P_2 \rangle$ when β_1 vanishes. The dashed (red) line is the power harvested by the first resistance $\langle P_1 \rangle$ when β_2 vanishes.